

Article

Effect of CeO₂-ZnO Nanocomposite for Photocatalytic and Antibacterial Activities

Asad Syed ^{1,*}, Lakshmi Sagar Reddy Yadav ^{2,3}, Ali H. Bahkali ¹, Abdallah M. Elgorban ¹ ,
Deshmukh Abdul Hakeem ⁴  and Nagaraju Ganganagappa ^{2,*}

¹ Department of Botany and Microbiology, College of Science, King Saud University, P.O. Box 2455, Riyadh 11451, Saudi Arabia; abahkali@ksu.edu.sa (A.H.B.); aelgorban@ksu.edu.sa (A.M.E.)

² Energy Materials Research Laboratory, Department of Chemistry, Siddaganga Institute of Technology, Tumkur 572103, India; lsr.yadav@gmail.com

³ Department of Chemistry, BMS Institute of Technology and Management, Bangalore 560064, India

⁴ Key Laboratory of Clean Chemistry Technology of Guangdong Regular Higher Education Institutions, School of Chemical Engineering and Light Industry, Guangdong University of Technology, Guangzhou 510006, China; abdulhakeem.desh@gmail.com

* Correspondence: assyed@ksu.edu.sa (A.S.); nagarajugn@rediffmail.com (N.G.)

Received: 29 June 2020; Accepted: 9 September 2020; Published: 16 September 2020



Abstract: The impact of a CeO₂-ZnO nanocomposite on the photocatalytic and antibacterial properties compared to bare ZnO was investigated. A CeO₂-ZnO nanocomposite was synthesized using *Acacia nilotica* fruit extract as a novel fuel by a simple solution combustion method. The obtained CeO₂-ZnO nanocomposite was confirmed structurally by XRD, FTIR, Raman and UV-DRS and morphologically by SEM/TEM analysis. The XRD pattern indicates the presence of both hexagonal Wurtzite-structured ZnO (major) and cubic-phase CeO₂ (minor). FTIR shows the presence of a Ce-O-Ce vibration at 468 cm⁻¹ and Zn-O vibration at 445 cm⁻¹. The existence of a band at 460 cm⁻¹ confirmed the F_{2g} Raman-active mode of the fluorite cubic crystalline structure for CeO₂. Diffused reflectance spectroscopy was used to estimate the bandgap (E_g) from Kubelka–Munk (K–M) theory which was found to be 3.4 eV. TEM analysis shows almost spherical-shaped particles, at a size of about 10–15 nm. The CeO₂-ZnO nanocomposite shows a good BET specific surface area of 30 m²g⁻¹. The surface defects and porosity of the CeO₂-ZnO nanocomposite caused methylene blue (MB) dye to degrade under sunlight (88%) and UV light (92%). The CeO₂-ZnO nanocomposite also exhibited considerable antibacterial activity against a pathogenic bacterial strain.

Keywords: cerium oxide; zinc oxide; combustion; photocatalytic degradation; antibacterial activity

1. Introduction

Research focuses on the photocatalytic degradation activity of organic dyes/industrial effluents have leading high priority for the simplification of poisonous and non-biodegradable organic/inorganic [1–3] materials using photocatalysts. These materials are unable to create more and more electron–hole pairs by the irradiation of light energy by retarding the electron–hole recombination property. To achieve high performance of photocatalytic degradation activity, catalysts should possess the optimum bandgap of a semiconducting property [4,5], such as ZnO [6] CeO₂ [7], TiO₂ [8] or Cu₂O [9]. These nanoscale materials also exhibit antibacterial activities that have greater significance towards the development of therapeutic products due to their environmental benignity [10].

CeO₂ is an n-type semiconductor metal oxide in which cerium belongs to the lanthanide group [11]. In applications, CeO₂ provides electromagnetic screens for anti-reflection coverings and is used in color TV tubes, glowing mantles, camera phone lenses, CD player lasers, ultra-modern chip systems and

solar cells, vehicle exhaust catalysts [12], biomedicine and photocatalysis. Nanostructured CeO₂ poses as the best UV absorber and is used as a preservative in polishes and coverings for wood additives to improve their UV stability. CeO₂ has been considered as an excellent semiconducting photocatalytic material due to its moderate band gap energy of 3.19 eV.

The redox couple of Ce³⁺/Ce⁴⁺ attracted its application towards heterogeneous catalysis, but it is limited to few. To overcome this existing problem, some synthetic strategies have been adopted to prepare the composite with metal or metal oxide. The formed composite possesses different physical and chemical properties from the individual metal oxides. There are many reports available on mixed metal oxides of CeO₂-TiO₂ to improve the photocatalytic performance. Various methods available to prepare nanostructural CeO₂ include hydrothermal, co-precipitation, microwave and solution combustion [13–16].

Nanostructured ZnO finds its applications in almost all the fields such as drug delivery, cosmetic, nutrients, gum, goods, picture, porcelain and crystal industries. The biological activity of ZnO is well known and the performances increase with the decrease in particle size and this can be observed under visible light [17]. The performance of ZnO is further enhanced by forming a composite with other metal oxides. ZnO shows a wide bandgap energy of 3.37 eV and belongs to *n*-type semiconductors used for short-wavelength optoelectronic devices [18]. ZnO-CeO₂ nanocomposites have been synthesized by various methods such as sol-gel, solvothermal, hydrothermal, photochemical reduction, co-precipitation, polymerization, laser ablation and sonochemical [19–26].

Compared with the above conventional methods, the combustion method provides an enhancement designed at producing nanomaterials in a simple way, that are less expensive, with more yield and high purity in the production of nanocrystalline single- or mixed-phase oxides [13]. The nanoparticle prepared using natural fuel shows significant enhanced properties compared to chemically prepared nanoparticles as discovered in the previous works. Here, some examples are given such as Pavithra et al. [27], who prepared ZnO nanoparticles by *Citrus maxima* (pomelo) juice which were used for electrochemical sensors, photodegradation activity and antibacterial properties. A.K. Ramasami et al. prepared ZnO nanoparticles by tapioca starch pearls which were used for antibacterial and photodegradation activities [28]. Rajith et al. prepared ZnO nanoparticles via the solution combustion method using *Calotropis gigantea* leaves extract as fuel and studied its biological and photocatalytic degradation activities [29]. Manjunath prepared ZnO nanoparticles by *Cajanus cajan* and studied its use in antibacterial and photodegradation activities [30]. Saipriya prepared CeO₂ nanoparticles by *Aloe barbadensis* miller gelas [16]. Mokkelbost prepared CeO₂ nanoparticles by Glycine [31] and studied its photocatalytic activity. Malleshappa prepared CeO₂ nanoparticles by Lucasaspera mediated as a fuel [32].

By combining the properties of CeO₂ and ZnO, the composite acts as an excellent photocatalytic material due to the increasing charge carrier mobility [33]. Therefore, in this study, photocatalytic degradation and antibacterial activities are analyzed for a CeO₂-ZnO nanocomposite synthesized using the natural fruit extract of *Acacia nilotica* as a fuel via the solution combustion method.

Acacia nilotica (L.) is an important ornamental and medicinal plant of tropical and sub-tropical regions, belongs to the family Fabaceae of the genus *Acacia*, commonly known as babul, and is a source of many active secondary metabolites which may serve as potential candidates for drug development with the greatest possibility of success in the near future. Ripened *Acacia nilotica* contains major proportions of phenolic derivatives in addition to crude protein, crude fiber, crude fat, carbohydrates, potassium, phosphorus, magnesium, iron and manganese in moderately high concentrations, and is also a source of cysteine, methionine, threonine, lysine and tryptophan. The fruit also contains mucilage and saponins [34,35].

This article reports the synthesis of a CeO₂-ZnO nanocomposite via a combustion method and its characterization using various analytical tools. The characterized CeO₂-ZnO nanocomposite can be used to study the photocatalytic and antibacterial activities.

2. Experimental

2.1. Materials

Analytical-grade (AR) chemicals cerium nitrate $\text{Ce}(\text{NO}_3)_3$ and zinc nitrate $\text{Zn}(\text{NO}_3)_2$ were purchased from Merck India Pvt. Ltd. No additional purification process has been carried out for the above-mentioned chemicals.

2.2. Extraction of Fuel from Fruits of *Acacia Nilotica*

Fresh fruits of *Acacia nilotica* were collected from near a forest located in Tumkur district, Karnataka. Fruits of *Acacia nilotica*, shown in Figure 1, were in the range of 7.5–15.0 cm in length. These were compressed and constricted at sutures with 8–12 seeds present per fruit. Of each fruit, 250 g was completely crushed and transferred to 1000 mL of distilled water. The mixture was boiled for one hour, and the resulting green solution was filtered and used as a fuel for combustion synthesis.



Figure 1. (a) *Acacia nilotica* tree, (b) fruits of *Acacia nilotica*.

2.3. Synthesis of CeO_2 - ZnO Nanocomposite

Equimolar (1:1) ratios of $\text{Ce}(\text{NO}_3)_3$ and $\text{Zn}(\text{NO}_3)_2$ were mixed with 30 mL of the prepared natural fruit extract, and the mixture was stirred for 10 min. The reaction mixture was heated on a hot plate to form a gel-like redox reaction mixture, which was then kept in a preheated muffle furnace maintained at ± 400 °C. Within 10 min, the reaction was completed by the smoldering flame type of reaction. The product was subjected to calcinations at 400 °C for 4 h, and the obtained white powder was subjected to characterization. Figure 2 explains the interaction of the ions between Ce^{3+} and Zn^{2+} and amino acids present in *Acacia nilotica*.

2.4. Characterization

A Shimadzu 700 X-ray diffractometer (XRD) with graphite-monochromatized $\text{Cu-K}\alpha$ (1.5418 Å) radiation was used to obtain the crystalline nature. The Fourier transform infrared (FTIR) spectrum of the prepared materials was analyzed with a Bruker Alpha-P spectrometer. A Shimadzu UV-1800 UV-Vis spectrometer was used to measure the UV-Vis absorption spectrum. A Hitachi 7000 scanning electron microscope (SEM) was used to examine the morphology of the samples. The Raman spectrum was recorded with the Peak Seeker Pro TM Raman system. The sample has been excited with an inbuilt 785 nm wavelength laser. The photoluminescence (PL) spectrum was examined by an Agilent Cary Eclipse Fluorescence spectrometer using a Xe lamp with an excitation wavelength of 397 nm. JEOL JEM 1200 Ex operating at 100 kV was performed using transmission electron microscopy (TEM).

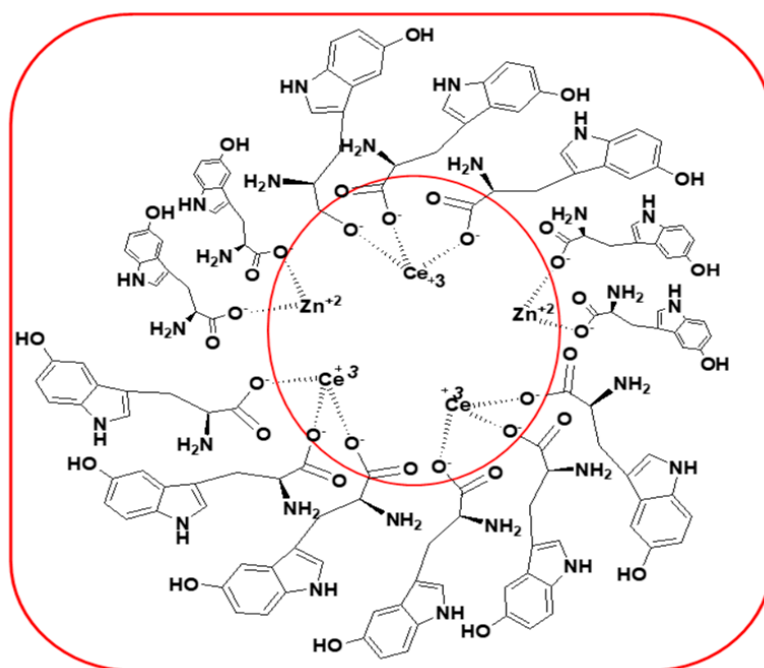


Figure 2. Interaction of ions between metals and amino acids.

2.5. Photocatalytic Experiment

The photocatalytic activity of CeO₂-ZnO and ZnO NPs was examined via degradation of MB dye in a photocatalytic reactor. The cylindrical photo-reactor contains a light source of UV lamp-250 W-365 nm having 75,200 lux, placed in the middle, surrounded by eight quartz reactor tubes of 100 mL capacity with a dimension of 37 cm height and 2.3 cm internal diameter together with cooling fans and an air bubbling unit.

In photocatalytic experiments, 200 mg of photocatalyst was mixed with a 100 mL of 5 ppm MB dye solution. This solution was stirred for 30 min before exposing it to the light source. After exposing the reaction mixture to the light, 2 mL of the aqueous sample was pipetted out at an interval of 30 min each and centrifugation was carried out for the removal of the catalyst. The degradation of MB dye was analyzed by the decrease in the MB concentration in the UV-Vis absorption spectrophotometer. The degradation efficiency was performed using Equation (1).

$$\text{Degradation efficiency} = [(C_0 - C_t)/C_0] \times 100$$

where C₀ and C_t are initial and final concentrations of the exposed dye solution.

3. Results and Discussion

3.1. XRD Analysis

Figure 3 shows the powder XRD pattern of the CeO₂-ZnO nanocomposite and ZnO NPs. The XRD analysis shows that ZnO had a pure single phase with a hexagonal wurtzite structure and well matches with the standard JCPDS card no. 5664. The cubic-structured CeO₂ was consistent with the standard JCPDS file no. 2-1306. The peak at 2θ = 28° indicates that CeO₂ was grown in a separate phase. ZnO and CeO₂ peaks overlap at 2θ = 47.5°, but we can make out the difference from the intensity of different phases assumed to be for the CeO₂ phase. The average crystallite sizes of the prepared CeO₂-ZnO nanocomposite (2θ = 31.4°, 34.6°, 36.4° and 47.4°) and ZnO NPs (2θ = 31°, 34.6°, 36° and 47.4°) calculated using the Debye-Scherrer equation were 7 and 12 nm, respectively.

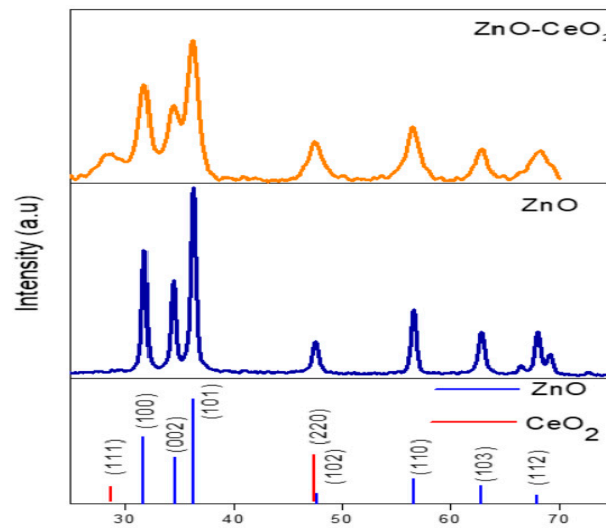


Figure 3. XRD pattern of CeO₂-ZnO and ZnO NPs with standard JCPDS.

The Debye–Scherrer formula used to determine the particle size is as follows.

$$D = 0.9\lambda / \beta \cos \theta \quad (1)$$

where D is the crystallite size, λ is the wavelength of X-ray radiation (1.5418 Å), β is the full-width half maximum of the diffraction peak and θ is the scattering angle.

3.2. FTIR Analysis

FTIR spectrum of the CeO₂-ZnO nanocomposite is shown in Figure 4. Hydroxyl (O-H) stretching and bending vibrations are centered at 3589 and 1630 cm⁻¹, respectively. A few additional absorption peaks observed at 1138, 950 and 708 cm⁻¹ explain the presence of trace amounts of fuel in the final product (CeO₂-ZnO nanocomposite). The bond at 468 cm⁻¹ corresponds to the Ce-O-Ce vibration mode and 445 cm⁻¹ is assigned to the Zn-O stretching vibration [36].

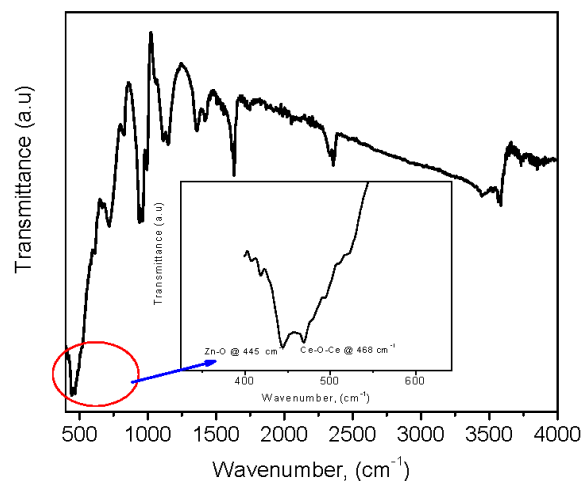


Figure 4. FTIR spectrum of CeO₂-ZnO NPs.

3.3. Raman Spectroscopy

Raman spectrum was elucidated by the structure of the CeO₂-ZnO nanocomposite (Figure 5) measured in the range of 300–800 cm⁻¹. The existence of a band at 460 cm⁻¹ confirmed the F_{2g} Raman-active mode of the fluorite cubic crystalline structure for CeO₂ [37,38].

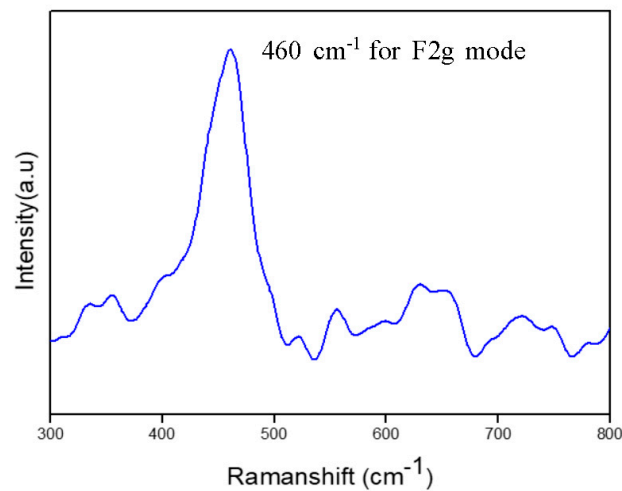


Figure 5. Raman spectrum of CeO₂-ZnO NPs.

3.4. Optical Properties

The UV-Vis DRS of the synthesized ZnO NPs and CeO₂-ZnO nanocomposite is shown in Figure 6. The strong band at 333 and 373 nm is attributed to the absorption of the host lattice of ZnO and the CeO₂-ZnO nanocomposite [26]. The bandgap (E_g) is estimated using the Kubelka–Munk (K–M) theory. The intercept of the tangents of the photon energy versus the $[F(R_\infty) h\nu]^{1/2}$ of ZnO and the CeO₂-ZnO nanocomposite gives the band gap. The K–M function $F(R_\infty)$ and photon energy ($h\nu$) are calculated by the following formula.

$$F(R_\infty) = (1-R)^2 / 2R_\infty \quad (2)$$

$$h\nu = 1240 / \lambda \quad (3)$$

where R_∞ is the reflection coefficient of the sample and λ is the absorption wavelength. The optical band gap (E_g) is calculated by

$$F(R) h\nu \cdot n = A(h\nu - E_g) \quad (4)$$

where $n = 2$ for a direct allowed transition and $n = \frac{1}{2}$ for an indirect allowed transition, A is constant and $h\nu$ is the photon energy. The obtained E_g values are 3.5 and 3.4 eV for ZnO NPs and the CeO₂-ZnO nanocomposite, respectively.

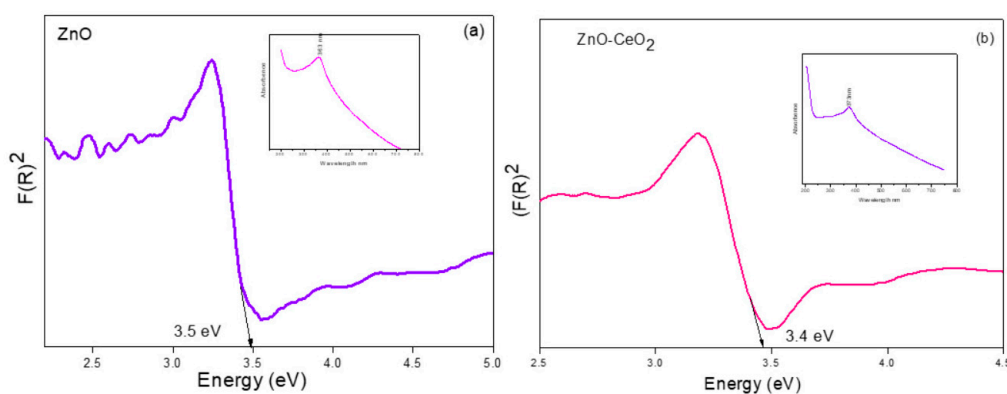


Figure 6. Band gap plots of (a) ZnO NPs (inset DRS graph) and (b) the CeO₂-ZnO (inset DRS graph) nanocomposite.

3.5. Photoluminescence Properties

Figure 7 shows the photoluminescence spectrum of the CeO₂-ZnO nanocomposite. The goal of the PL study was to determine deficiencies in the crystal structures of the nanomaterials. The ZnO NPs with numerous crystalline defects usually exhibit a PL band within the visible spectral region. In this case, we observed a high-intensity blue emission peak at approximately 479 nm from CeO₂ and peaks from the 479 to 575 nm region are due to the mixing of CeO₂ and ZnO luminescence. Orange emission at 594 nm and red emission at 716 nm are also observed for the CeO₂-ZnO NPs.

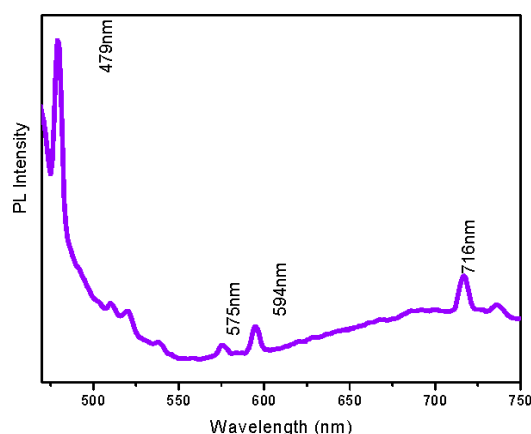


Figure 7. Photoluminescence spectrum of the CeO₂-ZnO nanocomposite.

3.6. SEM Analysis

Morphology of the CeO₂-ZnO nanocomposite is observed using SEM and is shown in Figure 8a,b. It is clear that the prepared CeO₂-ZnO nanocomposite is spongy and has a cave-like morphology, which shows that the prepared material is highly porous in its structure. The porous structure enhanced the surface area and thus exhibited good catalytic activity. The presence of Ce, Zn and O was analyzed by an EDS measurement of the CeO₂-ZnO nanocomposite (Figure 8c).

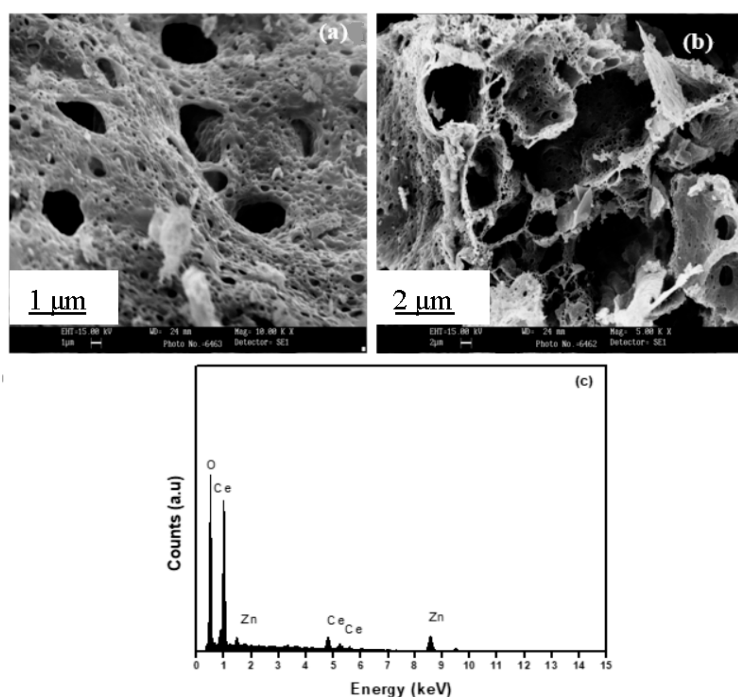


Figure 8. (a,b) SEM images and (c) EDS pattern of the CeO₂-ZnO nanocomposite.

3.7. TEM Analysis

Morphology, particle size and d-spacing are determined by TEM and HRTEM, as shown in Figure 9. Less agglomerated, almost spherical-shaped particles were observed (Figure 9a,c) and the average particle size was found to be 10–15 nm. HRTEM (Figure 9d) images and the SAED pattern (Figure 9d inset) clearly show a polycrystalline nature and the inter-planar distance matches with the ZnO and CeO₂ in the composite [39].

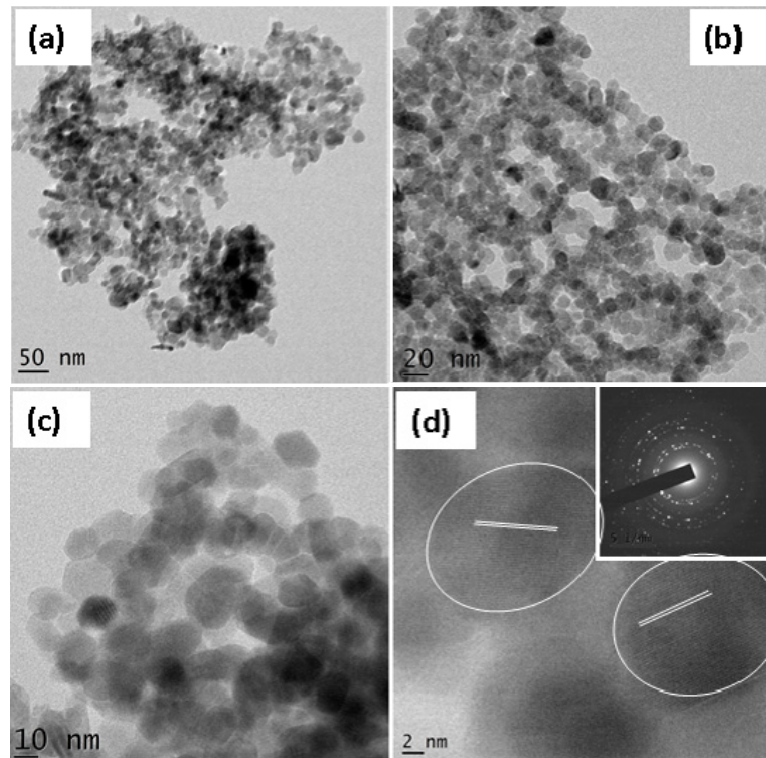


Figure 9. (a–c) TEM and (d) HRTEM (Inset: SAED pattern) images of the CeO₂-ZnO nanocomposite.

3.8. Surface Area Analysis from BET

Figure 10 shows the analysis of the surface area and pore size/distribution of the CeO₂-ZnO nanocomposite via the BET N₂ adsorption–desorption isotherm method. The N₂ adsorption–desorption isotherms of ZnO-CeO₂ display a H₄-type hysteresis loop and show a BET specific surface area of 30 m²g⁻¹ and a pore diameter of 3.3 nm [40].

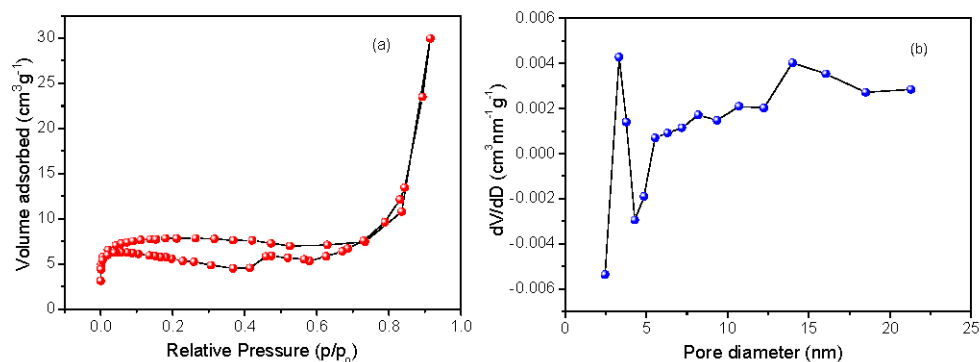


Figure 10. (a) N₂ adsorption–desorption isotherms and (b) pore size distribution of ZnO-CeO₂ nanocomposites.

3.9. Photocatalytic Properties

Figure 11 shows plots of the degradation percentage versus irradiation time of the synthesized ZnO and CeO₂-ZnO nanocomposite under UV- and sunlight irradiation. ZnO NPs (200 mg) reached 82 and 38% of MB dye (5 ppm) degradation under the UV- and sunlight, respectively. Conversely, it is noticed that there is a significant enhancement in the degradation of the CeO₂-ZnO (200 mg) nanocomposite over bare ZnO NPs. The CeO₂-ZnO nanocomposite (200 mg) shows 92% and 88% of degradation for MB dye (5 ppm) under the irradiations of UV- and sunlight, respectively, for a constant catalytic load. It evidently shows that the degradation of MB dye is more prominent in UV light than in sunlight [41–45].

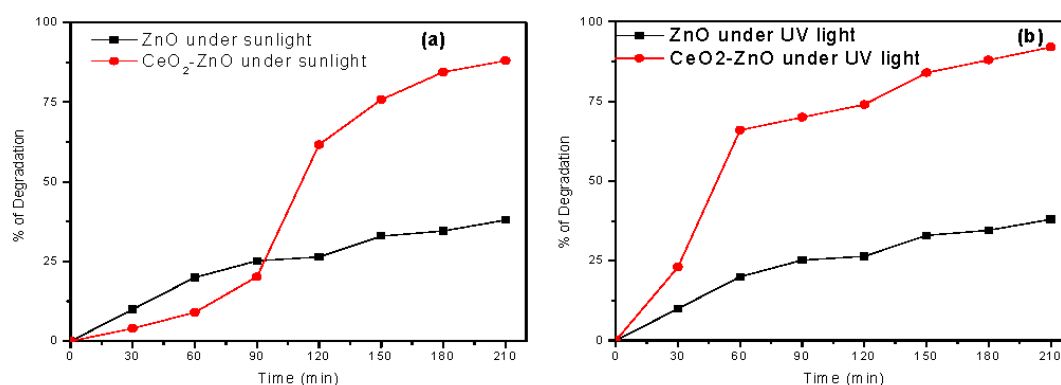
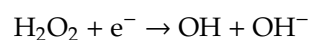
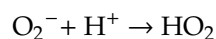
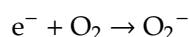
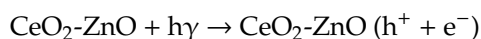


Figure 11. Photocatalytic degradation of MB dye of (a) ZnO and (b) CeO₂-ZnO NPs.

M. Faisal et al. reported a ZnO-CeO₂ nanocomposite for a smart chemical sensor and photocatalytic applications synthesized by a simple solution method. ZnO-CeO₂ achieved 92% of acridine orange and 80% of MB dye degradation after 170 min irradiation time. A. Taufik et al. prepared CeO₂-ZnO composites of various mole percentages with different heat treatment by the sol-gel method for photocatalytic applications. ZnO-CeO₂ (1:0.5) showed good degradation activity under visible light radiation. In this, they concluded that the photocatalytic activity decreases by the addition of sodium sulfate, ammonium oxalate and ter-butyl alcohol. Nidhi Shah et al. synthesized a CeO₂-ZnO composite via an in situ precipitation method without using any stabilizers via a sonochemical method and reported that the effectiveness of Rhodamine B (RhB) dye degradation by the sonochemical method is higher when compared to the other conventional methods of CeO₂-ZnO NPs.

With the above literature survey, and to the best of our knowledge, this work reveals that the green synthesized CeO₂-ZnO nanocomposite shows a high percentage of cationic dye degradation. It played an important role in avoiding the recombination of e⁻-h⁺ pairs and promoted the high excited energy states of electron-hole pairs [36–39].

The probable reaction mechanism expected during the photocatalytic degradation of MB dye was as follows [46,47].



3.10. Antibacterial Properties

The antibacterial properties of the CeO₂-ZnO nanocomposite are performed for Gram-negative *K. aerogenes* and Gram-positive *S. aureus* bacteria via the agar well diffusion method. The CeO₂-ZnO

nanocomposite showed countable antibacterial activity against *K. aerogenes* (500 $\mu\text{g}/50 \mu\text{L}$) bacterial strains. The bacterial strain inhibition zones of Gram-negative *K. aerogenes* and Gram-positive *S. aureus* bacteria and the 500 and 1000 μg concentrations of the $\text{CeO}_2\text{-ZnO}$ nanocomposite are shown in Figure 12 and their related data are listed in Table 1.

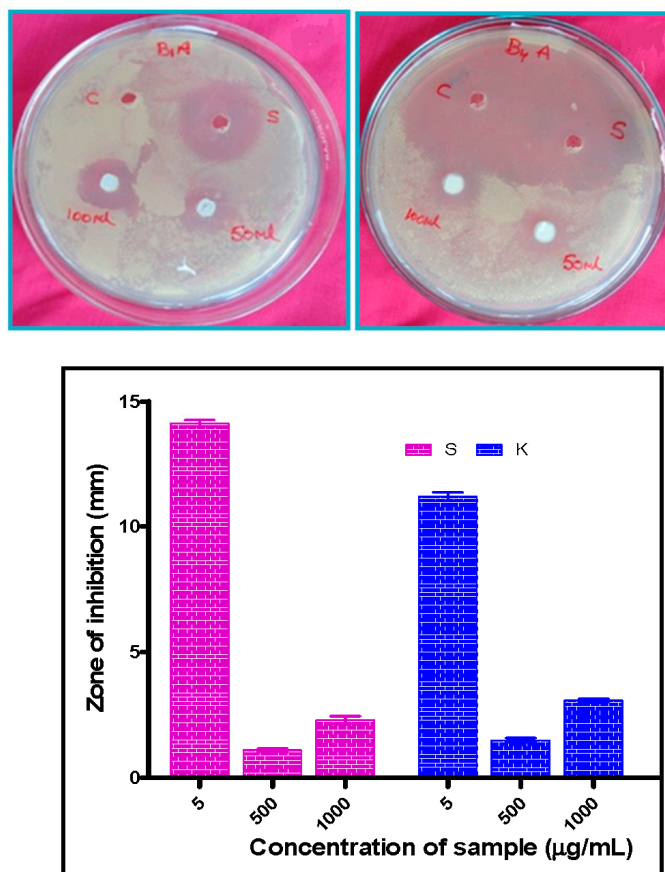


Figure 12. Zone of inhibition of pathogenic bacterial strains *K. aerogenes* (K) and *S. aureus* (S) for the $\text{CeO}_2\text{-ZnO}$ nanocomposite.

Table 1. Zone of inhibition of the $\text{CeO}_2\text{-ZnO}$ nanocomposite tested bacterial strains values.

Sl. No	Treatment	<i>K. Aerogenes</i> (K) (Mean \pm SE, mm)	<i>S. Aureus</i> (S) (Mean \pm SE, mm)
I	Standard (5 $\mu\text{g}/50 \mu\text{L}$)	11.17 \pm 0.17	14.13 \pm 0.13
II	$\text{CeO}_2\text{-ZnO}$ (500 $\mu\text{g}/50 \mu\text{L}$)	1.49 \pm 0.09	1.10 \pm 0.06
III	$\text{CeO}_2\text{-ZnO}$ (1000 $\mu\text{g}/100 \mu\text{L}$)	3.07 \pm 0.07	2.30 \pm 0.15

Note: the above values indicate the average \pm S.E. for three trails. Probable value less than 0.10 is assumed as significant.

The $\text{CeO}_2\text{-ZnO}$ nanocomposite exhibited better antibacterial performance than pure ZnO and CeO_2 . Furthermore, we studied the antibacterial effect of the $\text{CeO}_2\text{-ZnO}$ nanocomposite by antibacterial activity against Gram-negative and Gram-positive bacteria. Antibacterial results demonstrate that the nanocomposite significantly reduced the growth rate of bacteria.

4. Conclusions

CeO₂-ZnO nanocomposites were synthesized by the solution combustion method using *Acacia nilotica* fruit extract as the fuel. The average crystallite size of the prepared nanocomposite is 12 nm calculated using XRD data. The splitting of the band at a lower wavenumber, i.e., 468 cm⁻¹, corresponds to the Ce-O-Ce vibration and 445 cm⁻¹ is assigned to Zn-O stretching. The CeO₂-ZnO nanocomposite is spongy and has a cave-like structure, which indicates that it is highly porous in nature. HRTEM and SAED patterns indicate the polycrystalline nature. The CeO₂-ZnO nanocomposite exhibits a high percentage of methylene blue dye degradation by generating electron-hole pairs. The antibacterial properties of the CeO₂-ZnO nanocomposite are significant against Gram-positive bacterial strains.

Author Contributions: Conceptualization, N.G. and A.S.; methodology, L.S.R.Y.; software, L.S.R.Y. and A.S.; formal analysis, L.S.R.Y.; investigation, L.S.R.Y. and A.S.; resources, N.G.; data curation, L.S.R.Y., A.S. and N.G.; writing—original draft preparation, L.S.R.Y., A.S., A.M.E., D.A.H. and N.G.; writing—review and editing, A.S., L.S.R.Y., A.H.B. and N.G.; supervision, A.S., and N.G.; project administration, N.G.; funding acquisition, A.H.B. All authors have read and agreed to the published version of the manuscript.

Funding: Researchers Supporting Project number (RSP-2020/15) King Saud University, Riyadh, Saudi Arabia.

Acknowledgments: The authors extend their appreciation to the researchers supporting project number (RSP-2020/15) King Saud University, Riyadh, Saudi Arabia.

Conflicts of Interest: The authors declare no conflict of interest.

References

1. Zi-Qiang, X.; Hong, D.; Hang, C. Al-doping effects on structure, electrical and optical properties of c-axis orientated ZnO: Al thin films. *Mater. Sci. Semicond. Process.* **2006**, *9*, 132–135. [[CrossRef](#)]
2. Liu, Y.; Kanhere, P.D.; Wong, C.L.; Tian, Y.; Feng, Y.; Boey, F.; Wu, T.; Chen, H.; White, T.J.; Chen, Z.; et al. Hydrazine-hydrothermal method to synthesize three-dimensional chalcogenide framework for photocatalytic hydrogen generation. *J. Solid State Chem.* **2010**, *183*, 2644–2649. [[CrossRef](#)]
3. Neri, G.; Bonavita, A. Ethanol sensors based on Pt-doped tin oxide nanopowders synthesized by gel combustion. *Sens. Actuators B Chem.* **2006**, *117*, 196–204. [[CrossRef](#)]
4. Liang, Y.; Wicker, S.; Wang, X.; Erichsen, E.S.; Fu, F. Organozinc precursor-derived crystalline ZnO nanoparticles: Synthesis, characterization and their spectroscopic properties. *Nanomaterials* **2018**, *8*, 22–30.
5. Nie, L.; Zhang, Q. Recent progress in crystalline metal chalcogenides as efficient photocatalysts for organic pollutant degradation. *Inorg. Chem. Front.* **2017**, *4*, 1953–1962. [[CrossRef](#)]
6. Ewen, R.J.; Ratcliffe, N.M. Highly sensitive mixed oxide sensors for the detection of ethanol. *Sens. Actuators B Chem.* **2002**, *87*, 207–210.
7. Yamashita, H.; Nose, H. TiO₂ photocatalyst loaded on hydrophobic Si₃N₄ support for efficient degradation of organics diluted in water. *Appl. Catal. A Gen.* **2008**, *350*, 164–168. [[CrossRef](#)]
8. Nagaraju, G.; Shivaraju, G.C. Photocatalytic activity of ZnO nanoparticles: Synthesis via solution combustion method. *Mater. Today Proc.* **2017**, *4*, 11700–11705. [[CrossRef](#)]
9. Yadav, L.R.; Lingaraju, K.; Prasad, B.D.; Kavitha, C.; Banuprakash, G.; Nagaraju, G. Synthesis of CeO₂ nanoparticles: Photocatalytic and antibacterial activities. *Eur. Phys. J. Plus.* **2017**, *132*, 1–10.
10. Jung, S.M.; Lim, H.Y. Advanced photocatalytic activity using TiO₂/ceramic fiber-based honeycomb. *Stud. Surf. Sci. Catal.* **2010**, *175*, 441–444.
11. Xiong, L. Fast and simplified synthesis of cuprous oxide nanoparticles: Annealing studies and photocatalytic activity. *RSC Adv.* **2014**, *4*, 62115–62122. [[CrossRef](#)]
12. Hajipour, M.J.; Fromm, K.M. Antibacterial properties of nanoparticles. *Trends Biotechnol.* **2012**, *30*, 499–511. [[CrossRef](#)] [[PubMed](#)]
13. Yadav, L.R.; Nagaraju, G. Fruit juice extract mediated synthesis of CeO₂ nanoparticles for antibacterial and photocatalytic activities. *Eur. Phys. J. Plus.* **2016**, *131*, 54–61.
14. Rajesh, S.; Reddy, Y.L.S. Structural, optical, thermal and photocatalytic properties of ZnO nanoparticles of betel leave by using green synthesis method. *J. Nanostruct.* **2016**, *6*, 250–255.
15. Yadav, L.R.; Nagaraju, G. Synergistic effect of MgO nanoparticles for electrochemical sensing, photocatalytic-dye degradation and antibacterial activity. *Mater. Res. Express* **2017**, *4*, 25–28.

16. Ravishankar, T.N.; Nagaraju, G. Synthesis and characterization of CeO₂ nanoparticles via solution combustion method for photocatalytic and antibacterial activity studies. *Chemistry* **2015**, *4*, 146–154. [[CrossRef](#)] [[PubMed](#)]
17. Mishra, P.K.; Vaidya, B. Zinc oxide nanoparticles: A promising nanomaterial for biomedical applications. *Drug Discov. Today* **2017**, *22*, 1825–1834. [[CrossRef](#)]
18. Davis, K.; White, J. Band gap engineered zinc oxide nanostructures via a sol–gel synthesis of solvent driven shape-controlled crystal growth. *RSC Adv.* **2019**, *9*, 14638–14648. [[CrossRef](#)]
19. Wang, Z.L. Zinc oxide nanostructures: Growth, properties and applications. *J. Phys. Condens. Matter* **2004**, *16*, R829–R858. [[CrossRef](#)]
20. Zhong, Q.; Matijevic, E. Preparation of uniform zinc oxide colloids by controlled double-jet precipitation. *J. Mater. Chem.* **1996**, *6*, 443–447. [[CrossRef](#)]
21. Wang, L.; Muhammed, M. Synthesis of zinc oxide nanoparticles with controlled morphology. *J. Mater. Chem.* **1999**, *9*, 2871–2878. [[CrossRef](#)]
22. Bahnemann, B.W.; Hoffmann, M.R. Preparation and characterization of quantum size zinc oxide: A detailed spectroscopic study. *J. Phys. Chem.* **1987**, *91*, 3789–3798. [[CrossRef](#)]
23. Zhang, H.; Que, D. Synthesis of flower-like ZnO nanostructures by an organic-free hydrothermal process. *Nanotechnology* **2004**, *15*, 622–626. [[CrossRef](#)]
24. Zhang, J.; Yan, C. Control of ZnO morphology via a simple solution route. *Chem. Mater.* **2002**, *14*, 4172–4177. [[CrossRef](#)]
25. Li, W.J.; Shi, E.W. Hydrothermal preparation of nanometer ZnO powders. *J. Mater. Sci. Lett.* **2001**, *20*, 1381–1383. [[CrossRef](#)]
26. Chen, W.; Zhang, L. Sonochemical processes and formation of gold nanoparticles within pores of mesoporous silica. *J. Colloid Interface Sci.* **2001**, *238*, 291–295. [[CrossRef](#)]
27. Pavithra, N.S.; Lingaraju, K.; Raghu, G.K.; Nagaraju, G. Citrus maxima (Pomelo) juice mediated eco- friendly synthesis of ZnO nanoparticles: Applications to photocatalytic, electrochemical sensor and antibacterial activities. *Spectrochim. Acta Part. A: Mol. Biomol. Spectrosc.* **2017**, *185*, 11–19. [[CrossRef](#)]
28. Ramasami, A.K.; Nagabhushana, H.; Nagaraju, G. Tapioca starch: An efficient fuel in the gel-combustion synthesis of photocatalytically and anti-microbially active ZnO nanoparticles. *Mater. Charact.* **2015**, *99*, 266–276. [[CrossRef](#)]
29. Kumar, C.R.; Betageri, V.S.; Nagaraju, G.; Pujar, G.H.; Onkarappa, H.S.; Latha, M.S. Synthesis of core/Shell ZnO/Ag nanoparticles using calotropis gigantea and their applications in photocatalytic and antibacterial Studies. *J. Inorg. Organomet. Polym. Mater.* **2020**, in press. [[CrossRef](#)]
30. Manjunath, K.; RajaNaika, H.; Dupont, J.; Nagaraju, G. Facile combustion synthesis of ZnO nanoparticles using Cajanus cajan (L.) and its multidisciplinary applications. *Mater. Res. Bull.* **2014**, *57*, 325–334. [[CrossRef](#)]
31. Priya, G.S.; Kanneganti, A. Biosynthesis of cerium oxide nanoparticles using aloe barbadensis miller gel. *Int. J. Sci Res. Publ.* **2014**, *4*, 199–224.
32. Malleshappa, J.; Vidya, Y.S. Leucasaspera mediated multifunctional CeO₂ nanoparticles: Structural, photoluminescent, photocatalytic and antibacterial properties. *Spectrochim. Acta Part. A Mol. Biomol. Spectrosc.* **2015**, *149*, 452–462. [[CrossRef](#)]
33. Zak, A.K.; Ren, Z.F. Sonochemical synthesis of hierarchical ZnO nanostructures. *Ultrason. Sonochem.* **2013**, *20*, 395–400.
34. Taufik, A. Different heat treatment of CeO₂ nanoparticle composited with ZnO to enhance photocatalytic performance. *IOP Conf. Series Mat. Sci. Eng.* **2017**, *188*, 012–038.
35. Lin, F.; Alxneit, I.; Wokaun, A. Structural and chemical changes of Zn-doped CeO₂ nanocrystals upon annealing at ultra-high temperatures. *Cryst. Eng. Commun.* **2015**, *17*, 1646–1653. [[CrossRef](#)]
36. Faisal, M.; Abdullah, M.M. Smart chemical sensor and active photo-catalyst for environmental pollutants. *Chem. Eng. J.* **2011**, *173*, 178–184. [[CrossRef](#)]
37. Ramasamy, V.; Vijayalakshmi, G. Effect of Zn doping on structural, optical and thermal properties of CeO₂ nanoparticles. *Superlattices Microstruct.* **2015**, *85*, 510–521. [[CrossRef](#)]
38. Tju, H.; Shabrany, H. Degradation of methylene blue (MB) using ZnO/CeO₂/nanographene platelets (NGP) photocatalyst: Effect of various concentration of NGP. *AIP Conf. Proce.* **2017**, *1862*, 030037-5.
39. Prabhu, S.; Viswanathan, T.; Jothivenkatachalam, K.; Jeganathan, K. Visible Light Photocatalytic Activity of CeO₂-ZnO-TiO₂ Composites for the Degradation of Rhodamine, B. *Indian J. Mat. Sci.* **2014**, *536123*, 1–10. [[CrossRef](#)]

40. Deepa, K.; Venkatesh, T.V. Synthesis of CeO₂ doped ZnO nanoparticles and their application in Zn-composite coating on mild steel. *Arab. J. Chem.* **2020**, *13*, 2309–2317.
41. Faisal, M.; Abdulla, M.M. Role of ZnO-CeO₂ Nanostructures as a Photo-catalyst and Cheema-sensor. *J. Mater. Sci. Technol.* **2011**, *27*, 594–600. [[CrossRef](#)]
42. Sahar, M.; Ghada, M.M.; Nady, A.F.; Gehan, A.F. Effect of nanosize CeO₂ or ZnO loading on adsorption and catalytic properties of activated carbon. *Adsorp. Sci. Technol.* **2017**, *35*, 774–788.
43. Anushree; Kumar, S.; Sharma, C. Synthesis, characterization and catalytic performance of ZnO–CeO₂ nanoparticles in wet oxidation of wastewater containing chlorinated compounds. *Appl. Nanosci.* **2017**, *7*, 567–575. [[CrossRef](#)]
44. Lan, S.; Sheng, X. Modification of antibacterial ZnO nanorods with CeO₂ nanoparticles: Role of CeO₂ in impacting morphology and antibacterial activity. *Colloid Interf. Sci. Commun.* **2018**, *26*, 32–38. [[CrossRef](#)]
45. Qiao, X.Q.; Zhang, Z.W.; Li, Q.H.; Hou, D.; Zhang, Q.; Zhang, J.; Li, D.S.; Feng, P.; Bu, X. In situ synthesis of n–n Bi₂MoO₆ & Bi₂S₃ heterojunctions for highly efficient photocatalytic removal of Cr 6. *J. Mater. Chem. A* **2018**, *6*, 22580–22589.
46. Zhu, L.; Li, H.; Xia, P.; Liu, Z.; Xiong, D. Hierarchical ZnO decorated with CeO₂ nanoparticles as the direct Z-Scheme heterojunction for enhanced photocatalytic activity. *ACS Appl. Mater. Interfaces* **2018**, *10*, 39679–39687. [[CrossRef](#)]
47. Saravanan, R.; Mohammad, M.K.; Khan, F.G.; Jiaqian, Q.; Vinod, K.G.; Stephen, A. Ce³⁺ - ion-induced visible-light photocatalytic degradation and electrochemical activity of ZnO/CeO₂ nanocomposite. *Sci. Rep.* **2016**, *6*, 31641–31642.



© 2020 by the authors. Licensee MDPI, Basel, Switzerland. This article is an open access article distributed under the terms and conditions of the Creative Commons Attribution (CC BY) license (<http://creativecommons.org/licenses/by/4.0/>).